British Geological Survey

Reviewing the relations of seismic velocities and electrical resistivity with the temperature of high-enthalpy geothermal reservoirs with an example from an East African rift volcano

BGS IGRD PROJECT

Open Report OR/23/030

BRITISH GEOLOGICAL SURVEY

IGRD PROJECT

OPEN REPORT OR/23/030

Reviewing the relations of seismic velocities and electrical resistivity with the temperature of high-enthalpy geothermal reservoirs with an example from an East African rift volcano

Xiaoyang Wu, Brian Baptie, Juliane Huebert, Ciaran Beggan

Keywords

Geothermal, seismic velocities, electrical resistivity, rock physics models, temperature.

Bibliographical reference

X.WU, B. BAPTIE, J. HUEBERT & C. BEGGAN, 2023. *British Geological Survey Internal Report*, OR/23/030. 26pp.

Keyworth, Nottingham British Geological Survey 2023

BRITISH GEOLOGICAL SURVEY

The full range of our publications is available from BGS shops at Nottingham, Edinburgh, London and Cardiff (Welsh publications only) see contact details below or shop online at www.geologyshop.com

The London Information Office also maintains a reference collection of BGS publications, including maps, for consultation.

We publish an annual catalogue of our maps and other publications; this catalogue is available online or from any of the BGS shops.

The British Geological Survey carries out the geological survey of Great Britain and Northern Ireland (the latter as an agency service for the government of Northern Ireland), and of the surrounding continental shelf, as well as basic research projects. It also undertakes programmes of technical aid in geology in developing countries.

The British Geological Survey is a component body of UK Research and Innovation.

British Geological Survey offices

Nicker Hill, Keyworth,
Nottingham NG12 5GG
Tel 0115 936 3100

BGS Central Enquiries Desk
Tel 0115 936 3143
email enquiries@bgs.ac.uk

BGS Sales
Tel 0115 936 3241
email sales@bgs.ac.uk

The Lyell Centre, Research Avenue South,
Edinburgh EH14 4AP
Tel 0131 667 1000
email scotsales@bgs.ac.uk

Natural History Museum, Cromwell Road,
London SW7 5BD
Tel 020 7589 4090
Tel 020 7942 5344/45
email bgslondon@bgs.ac.uk

Cardiff University, Main Building, Park Place,
Cardiff CF10 3AT
Tel 029 2167 4280

Maclean Building, Crowmarsh Gifford,
Wallingford OX10 8BB
Tel 01491 838800

Geological Survey of Northern Ireland, Department for the Economy, Dundonald House, Upper Newtownards Road, Ballymiscaw, Belfast, BT4 3SB
Tel 0289 038 8462
www2.bgs.ac.uk/gsni/

Natural Environment Research Council, Polaris House, North Star Avenue, Swindon SN2 1EU
Tel 01793 411500 Fax 01793 411501
www.nerc.ac.uk

UK Research and Innovation, Polaris House,
Swindon SN2 1FL
Tel 01793 444000
www.ukri.org

Website www.bgs.ac.uk
Shop online at www.geologyshop.com

Contents

Summary

High-enthalpy geothermal reservoirs have been widely explored as they can potentially provide exceptional energy productivity and efficiency. However, there remain unresolved questions about how to characterise these reservoirs from surface measurements, which at present preclude a better understanding of the physical properties of such heat-bearing rocks with saturated/injected fluids. This report aims to summarise the available rock physics modelling approaches for elucidating the electrical and seismic properties of geothermal reservoirs and high-temperature fluids, and to provide solutions for estimating the temperature distribution of high-enthalpy reservoirs, particularly those related to magma storage reservoirs in volcanic regions. We revisit the empirical relations including the Horner plot method and the commonly used resistivity-temperature relation to define the empirical relationship between temperature and electrical or seismic properties observed with geophysical sounding techniques. The report also introduces the methods that relate conductivity to elastic properties through porosity and the cross-properties Differential Effective Medium (DEM) method, which establishes the conductivity/resistivity–seismic velocity relationship directly, allowing the calculation of one physical property from another more easily measured one. We use Burgers model to numerically model the frequency-dependent shear modulus of linear viscoelastic media, where the steady-creep effect in the rock frame is caused by high temperatures and the Arrhenius equation is used to link viscosity with temperature. Finally, we demonstrate the use of rock physics modelling techniques to estimate geothermal gradient from 1-D seismic velocities obtained from inversions of earthquake data and study the resistivity and velocity relations at Aluto, a stratovolcano in the Central Main Ethiopian Rift, part of the East African Rift. Geothermal exploration at Aluto started in the 1970s and it is the site of Ethiopia's first geothermal electric power plant. Both passive seismic and magnetotelluric (MT) surveys have been conducted in the region to help understand the subsurface structure and repeated episodes of volcanic unrest. In the report, we attempt to summarize and combine different rock physics models to characterize high-enthalpy geothermal systems for their elastic and electrical properties. We do this to facilitate joint inversion of geophysical data to better identify zones of high geothermal energy potential that might be economically useful for renewable energy production in the Ethiopian rift and elsewhere.

Introduction

1.1 REVIEW OF HIGH ENTHALPY GEOTHERMAL RESERVOIRS

Geothermal energy can provide competitive, low-carbon power to help meet global CO2 reduction targets and accelerate the decarbonisation of the energy sector. High-enthalpy geothermal systems (T>160°C) have been paid special attention due to their high energy potential not only for providing heat but also for electric power generation (via steam turbine). Systems with temperatures above 250°C are almost always associated with volcanic activity, with elevated temperature gradients resulting from high heat flow caused by shallow intrusions of magma (Reinsch et al., 2017). In zones close to the magma chamber, fluids may reach the supercritical state, circa. T > 374°C and P > 22.1 MPa for pure water, T > 406 °C, and P > 29.8 MPa for seawater, which can provide more energy productivity and efficiency, but pose challenges for drilling techniques due to their high erosivity. The superhot rock may also exhibit ductile properties at such high temperatures. Understanding the elastic stiffness and deformation mechanism of superhot rock is crucial for the geophysical exploration of such geothermal reservoirs.

Geophysical methods such as seismic survey and magnetotelluric (MT) are effective tools in identifying high enthalpy geothermal reservoirs. Seismic measurements can be

used to characterize the anelastic behaviour and brittle-ductile property of superhot rocks with varying permeability/saturation. Carcione et al. (2006) developed a theoretical approach to characterise the steady-state creep when drilling through rock salt using the Burgers model, which was then utilised to simulate the seismic waves in the brittle-ductile transition of the Earth's crust (Carcione and Poletto, 2013; Carcione et al., 2014). A series of studies have been conducted to combine the Burgers model with different rock physics models (Carcione et al., 2016; Carcione et al., 2018a; Carcione et al., 2018b) to characterise fluid effects in high-temperature porous media and geothermal reservoirs (Poletto, et al. 2018; Farina et al., 2019; Poletto et al., 2019). Resistivity logging, transient electromagnetic (TEM) or MT data are used to detect superhot hydrothermal reservoirs, identify conductive clay layers that cover the geothermal systems, and image fluid saturated host rocks or partially melted subvolcanic magma chambers (Samrock et al., 2015). A conceptual model was developed by Johnston, Pellerin and Hohmann (1992) and Cumming and Mackie (2007) to describe the temperature pattern, alteration zones and resistivity distribution for high-enthalpy geothermal systems.

The East African Rift system is recognised as a region that is rich in geothermal energy resources that could provide a reliable, affordable and local source of renewable energy to help meet the energy demands in countries like Ethiopia across the region (IRENA, 2020). Aluto in the Main Ethiopian Rift Valley is currently the only producing geothermal field in central Ethiopia. It has produced electricity since 1990 and has recently undergone expansion to increase production (Samrock et al., 2020). Both passive seismic and MT surveys have been carried out in the region to help understand repeated episodes of volcanic unrest. As a result, a wide variety of data are available to help test the applicability of new geophysical methods to identify areas of high geothermal potential.

Wilks et al. (2017) located passive seismic events detected by a local network of 12 seismometers deployed at the Aluto Volcano in Ethiopia from 2012 to 2014 and analysed the focal depths and mechanisms. Wilks et al. (2020) used local earthquake tomography with the same data to model the 3D seismic velocity structure beneath Aluto. They subdivided the regions beneath the volcanic edifice into four zones: (1) a shallow zone (-2 to 0 km above mean sea level) of high seismicity that corresponds to the hydrothermal system and is influenced by a high fluid saturation and circulation; (2) a relatively aseismic zone (0 to 2 km) that is impermeable to ascending volatiles; (3) a region of increased fluid-induced seismicity (2 to 9 km) that is driven by magmatic intrusion from below and (4) a deeper zone (below 9 km) that is interpreted as a partially crystalline magmatic mush.

Samrock et al. (2015) conducted a resistivity inversion of MT data from the Aluto-Langano geothermal field to construct a 3D resistivity model of the subsurface and identify the low resistivity zone associated with clay alteration cap rock zones (Cherkose et al., 2018; Samrock et al., 2020). The result was used to identify three main resistivity structures: (1) a high-resistivity layer associated with unaltered volcanic rocks at shallow depths, (2) a low-resistivity layer related to argillic alteration clay products, and (3) a gradually increasing high-resistivity region at greater depths related to the formation of high-temperature alteration minerals. In contrast, Huebert et al. (2018) developed a regional 2-D model of electrical resistivity of the crust based on MT data along a 110 km transect across the central Main Ethiopian Rift but found no evidence of a highly conductive region associated with a magma chamber directly under the central rift volcano Aluto.

Jones (2020) developed a 2D regional heat flow map for the East African Rift using heat flow and geothermal gradient data from boreholes and lake-bottom probe measurements to identify regions of geothermal interest. In addition to geophysical data sets, direct observations from several boreholes are available. Gebru et al. (2021) estimated the natural state formation temperatures (before the commencement of production drilling) from five boreholes in the Aluto-Langano Geothermal Field using the Horner(1951) plot method, which is a popular method to estimate formation temperature from downhole logging temperature data. A temperature cross-section was interpolated from these boreholes to help identify the location of the hot up-flow zone in the geothermal reservoir.

1.2 REVIEW OF ROCK MODELS RELATING TEMPERATURE TO OTHER ROCK PARAMETERS

Understanding the effect of temperature on the physical properties of rocks containing saturated fluids is important for geothermal resource exploration. The empirical relations between velocities/elastic moduli and temperature can be negatively linear (Iovenitti et al., 2013; Yin et al., 2021), polynomial or exponential (Mendrinos et al., 2022). Derivation of empirical relations from laboratory measurements or drilling data for a specific geothermal area can be used to estimate the temperature field from inverted seismic/electromagnetic properties.

The properties of rock and its saturated fluids are strongly influenced by temperature, which lead to different geophysical responses. Batzle and Wang (1992) summarised the empirical relations for pore fluids properties such as density, bulk modulus, velocity and viscosity with temperature and pressure, and discussed their application in hydrocarbon exploration. Ciz and Shapiro (2007) developed a generalization of Brown and Korringa's and Gassmann equations for a solid infill of the pore space based on the elastic/viscoelastic correspondence principle (Hashin, 1970). Ciz et al. (2009) further extended this model to calculate the elastic properties of rocks saturated with heavy oil, where the temperature effect was incorporated following Beggs and Robinson (1975)'s relationship between the low-frequency viscosity and temperature for a viscoelastic material. Jaya et al. (2010) included the temperature effect in the Gassmann (1951) equation by considering the temperature dependence of the saturating fluid bulk modulus and density. Pore microstructures can also be influenced by temperature and pressure and hence affect the elastic property of porous rocks. The Mori and Tanaka (1973), David and Zimmerman (2011) models have been widely used to correlate the elastic moduli with pressure-induced pore and microcrack shape change in a rock. Yuan, Han and Zhang (2016) developed a rock physics model that integrated solid oil into the sand frame, with temperature-dependent moduli. Qi et al. (2021) developed a temperature-dependent double-porosity model based on Biot's theory, which takes the temperature dependence of the four parameters: pore fluid density, fluid viscosity, fluid bulk modulus and porosity into account. Yang et al. (2022) developed a correlation of dynamic shear and bulk modulus of porous rocks with temperature and pressure to the characteristics of the microstructure of porous media.

Our aim is to investigate how these different rock physics models can be applied to high-enthalpy geothermal reservoir rocks, where pore geometry and porosity are likely to play a big part in determining the seismic velocity, whereas for the electrical resistivity, the free electrons and fluid content will be more important. We also want to investigate how to take advantage of the result from joint MT and seismic inversion and link them with temperature by using rock physics models. Specifically, we combine Burgers model with Arrhenius equation to estimate the frequency-dependent shear

modulus of linear viscoelastic media and apply them to estimate the geothermal gradient from seismic velocity in Aluto geothermal field. We also study the cross-properties Differential Effective Medium (DEM) method(Cilli and Chapman, 2021), which is used to estimate conductivity from elastic properties and vice versa.

Empirical relationships between conductivity/resistivity and seismic velocity can be useful when one property can be measured more easily than the other. One approach to establish such a relationship is to combine the relations of both properties with a common property such as porosity, e.g., using Archie's law and Gassmann's equation. Carcione et al. (2007) gave an overview of different rock physics models for the calculation of electrical conductivity, stiffness moduli, and density for different rock frames with/without fluid content and developed the cross-property relations between conductivities and velocities. Werthmüller et al. (2013) used a Gassmann's relation for the conversion from velocity to porosity, and the self-similar model (Sen et al., 1981) for the conversion from porosity to resistivity. Then the model was updated from depth and anisotropy information and used to predict Controlled-Source ElectroMagnetic (CSEM) responses within a Bayesian framework to account for the uncertainties (Werthmüller et al., 2014). This provided a good starting model for CSEM inversion and joint inversion. Han, Wei, and Li (2020), Cilli and Chapman (2020, 2021) utilised the Differential Effective Medium (DEM) theory that relates elastic and electrical properties to porosity and pore aspect ratio to establish such cross-property relations. Their methods were used to estimate seismic velocities and V_P/V_S ratio as a function of conductivity for both clean sandstones and clay-bearing sandstones from laboratory-measured data (Han et al., 2011). In the following, we will review some of the mentioned models and investigate them for the applicability to a high-enthalpy geothermal reservoir.

Empirical relations and rock physics modelling

2.1 FINDING THE RESERVOIR TEMPERATURE USING THE HORNER PLOT METHOD

Gebru et al. (2021) applied the Horner plot method which uses the measured temperature at a given depth from several temperature logs taken at different times to extrapolate the formation temperature before production drilling. It is based on the 1D heat conduction equation as shown in Equation (1), which describes the temperature T as a partial differential equation of time *t* and position/space *x*,

$$c_p \rho \frac{\partial T}{\partial t} = k \frac{\partial^2 T}{\partial x^2} \qquad (1)$$

where c_p is the heat capacity of the material (J/(kg·K)), ρ is the density (kg/m^3), k is the thermal conductivity(W/(m·K)). From Equation (1), we know that temperature and time are linearly correlated at a fixed depth, the Horner time (τ) is given by Equation (2),

$$\tau = \frac{\Delta t}{\Delta t + t_c} \qquad (2)$$

Where t_c is the total circulation time before borehole shut-in (hrs); Δt is each observation time minus the time that circulation was stopped (hrs). We can obtain the formation temperature by plotting the logarithm of the Horner time τ against the measured temperature at a fixed depth as shown in Figure 1. Then the intercept of the straight line with y-axis indicates the formation temperature.

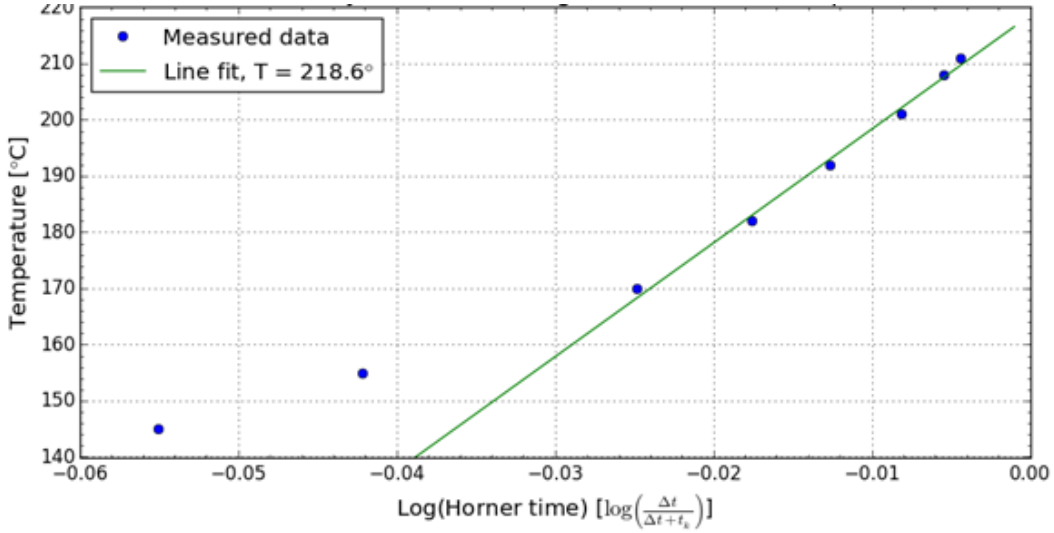

Figure 1 Example of a Horner Plot to estimate formation temperature from Figure 2 of Gebru et al. (2021). When Δt increases, the measured temperature will close to the formation temperature as shown T=218.6°C.

2.2 AN EMPIRICAL RESISTIVITY-TEMPERATURE RELATION

When the pore fluid conductivity is much greater than the porous rock conductivity, the rock resistivity is inversely proportional to the fluid conductivity, porosity and fluid saturation according to the Archie's law (1942). Under such a case, the strata resistivity and temperature are generally inversely correlated and can be expressed by the following equation (Dakhnov,1962),

$$\rho_t = \rho_0 / [1+\alpha(T-T_0)] \qquad (3)$$

where ρ_0 is the resistivity at temperature T_0; ρ_t is the resistivity at temperature T; α is the rock temperature coefficient, which can be determined using prior information from drilling data. Then, the geothermal reservoir temperature can be estimated by transforming Equation (3) into,

$$T = T_0 + (\rho_0/\rho_t - 1)/\alpha \qquad (4)$$

where ρ_0 at T0 for a certain lithology can be measured in the laboratory. ρ_t can be obtained from the MT data inversion. The subsurface needs to be divided into different areas in terms of lithological distribution. Zhao et al. (2022) utilised this relationship to estimate the temperature and depth of geothermal reservoirs from Controlled-Source Audio-frequency Magnetotellurics (CSAMT) resistivity.

2.3 THE ELECTRICAL–ELASTIC CORRELATIONS BASED ON POROSITY

Following Carcione et al. (2007), the dry-rock elastic moduli can be assumed as a function of porosity, i.e., bulk modulus $K_m(\phi)$ and shear modulus $\mu_m(\phi)$. Then, ϕ as a function of conductivity $\phi(\sigma)$ is replaced in the Gassmann equation, providing a simple model to estimate fluid saturation effect on bulk modulus. The relation between the bulk modulus of the saturated rock, K, and the porosity, ϕ, is given by,

$$K = K_G = \frac{K_s - K_m(\phi) + \phi K_m(\phi)(\frac{K_s}{K_f} - 1)}{1 - \phi - \frac{K_m(\phi)}{K_s} + \phi\frac{K_s}{K_f}}, \qquad (5)$$

where K_m and μ_m are the bulk and shear moduli of the matrix, and K_s and K_f are the grain and fluid bulk moduli, respectively. The model of Krief et al. (1990) can be used to obtain the dry-rock moduli K_m and μ_m as a function of porosity ϕ. ϕ has the following relations with σ in terms of different rock physics models (Carcione, 2007),

Archie's Law (Archie, 1942) gives the porosity as a function of the conductivities of the fluid-saturated clean sand, σ, and the pore fluid, σ_f, as

$$\phi = \left(\frac{\sigma}{\sigma_f}\right)^{1/m}, \qquad (6)$$

where m is the cementation exponent of the rock. The model of Hermance (1979) is a particular case of the Bussian (1983) model, which considers explicitly the conductivity of the clay particles σ_s in sandstone with clay,

$$\phi = \left(\frac{\sigma - \sigma_s}{\sigma_f - \sigma_s}\right)^{1/m}, \qquad (7)$$

where σ is the resistivity of the fluid-saturated solid rock. The complex refraction-index method (Schön, 1996) derives σ using the electromagnetic ray approximation.

$$\phi = \left(\frac{\sigma^{1/\gamma} - \sigma_s^{1/\gamma}}{\sigma_f^{1/\gamma} - \sigma_s^{1/\gamma}}\right), \gamma = 2, \qquad (8)$$

γ is the complex refraction-index. For two constituents solid and fluid, the porosity is given by the following expression in the self-similar model (Sen et al., 1981),

$$\phi = \left(\frac{\sigma - \sigma_s}{\sigma_f - \sigma_s}\right)\left(\frac{\sigma_f}{\sigma}\right)^{1-1/m}, \qquad (9)$$

The Glover et al.(2000) model has the form

$$\sigma = (1 - \phi)^p \sigma_s + \sigma_f \phi^m, \qquad (10)$$

p is a representative exponent related to m.The Hashin-Strikman (HS) lower and upper bound of porosity for a system of two components (solid and fluid) (Berryman, 1995) can be expressed as,

$$\phi = \left(\frac{\sigma_s - \sigma}{\sigma_s - \sigma_f}\right)\left(\frac{\sigma_f + 2\sigma_s}{\sigma + 2\sigma_s}\right), \qquad (11)$$

$$\phi = \left(\frac{\sigma_s - \sigma}{\sigma_s - \sigma_f}\right)\left(\frac{3\sigma_f}{\sigma + 2\sigma_f}\right), \qquad (12)$$

Table 1. Material properties for subcritical brine saturation, adapted from Carcione et al. (2007).

Rock	σ_s	σ_f	K_s	μ_s	ρ_s	K_f	ρ_f
sandstone-brine	10^{-3}	0.01, 0.1	39	40	2.65	2.25	1

In hydrothermal reservoirs, the conductivity of fresh water/saline varies dramatically with temperature and pressure, which determine the aggregate state of water, which itself may vary from liquid to steam or be in a supercritical phase. The conductivity of brine has a tendency to increase with temperature at subcritical conditions. At supercritical conditions, the removal of charge carriers from the brine causes a reduction of conductivity by an order of magnitude (Kummerow et al., 2021). This provides us with a clue to set the value of conductivity for water at supercritical state and subcritical state.

The seven cases as shown in Equations (6)-(12) have been used to describe the conductivity-bulk modulus relations of the brine-saturated sandstone. We use two values for the conductivity of fluid 0.01 S/m and 0.1 S/m as shown in Table 1 to see how the variation of fluid conductivity at subcritical conditions affect the cross relations. Figure 2 shows the modelling results. We can see that HS upper bound estimates the highest value conductivity for saturated rock. For a two-material composite, the HS upper bound is realised when the stiffer material forms the shell of spheres and the softer material fills the core, and vice versa for the HS lower bound. At a higher contrast between fluid and rock conductivity, as shown in Figure 2 (c) and (d), the Hermance, the complex refraction-index method, self-similar, and Glover models are all within the HS upper and lower bound.

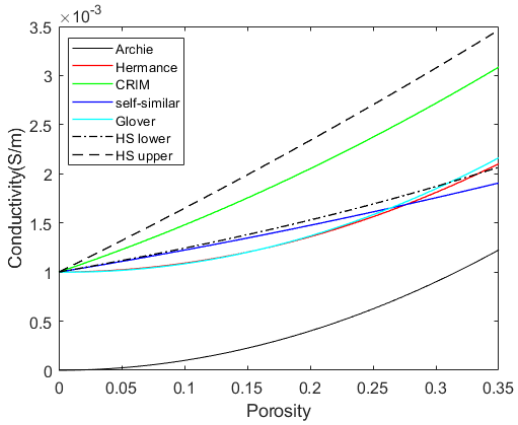

(a) Porosity-conductivity relation at σ_f = 0.01 S/m.

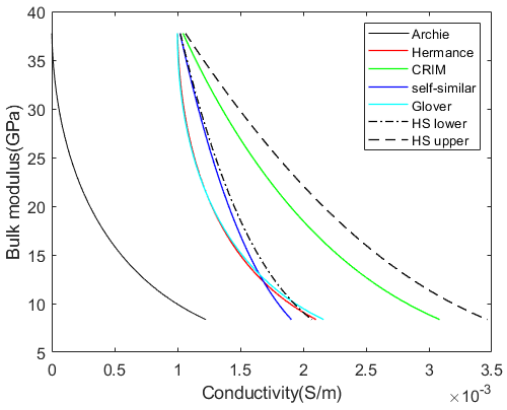

(b) Conductivity-bulk modulus relation at σ_f = 0.01 S/m.

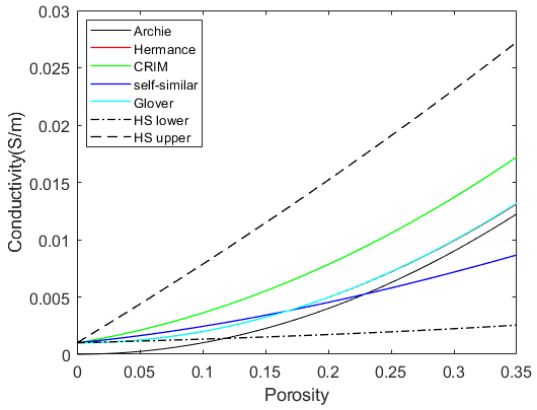

(c) Porosity-conductivity relation at σ_f = 0.1 S/m.

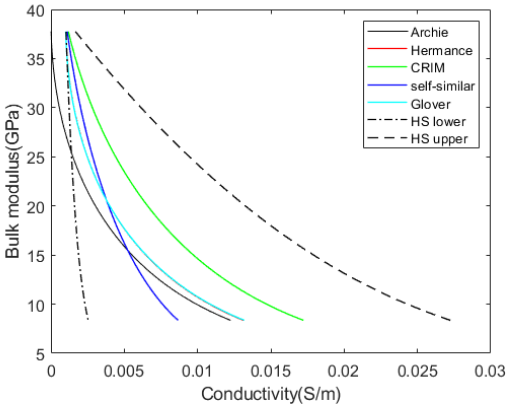

(d) Conductivity-bulk modulus relation at σ_f = 0.1 S/m.

Figure 2. The porosity-conductivity and conductivity-bulk modulus relations of brine-saturated sandstone.

2.4 ELECTRICAL–ELASTIC MODELLING USING CROSS-PROPERTY DEM

Han et al. (2011) and Cilli and Chapman (2021) proposed that the cross-property DEM can be expressed as a set of coupled differential equations that relate the electrical and elastic properties of a two-phase, isotropic, linearly elastic, electrically conductive composite:

$$\frac{dK^*}{d\sigma^*} = \frac{1}{3\sigma^*}\left(\frac{K_2 - K^*}{\sigma_2 - \sigma^*}\right)\frac{P^{(*2)}}{R^{(*2)}} \qquad (13)$$

$$\frac{d\mu^*}{d\sigma^*} = \frac{1}{3\sigma^*}\left(\frac{\mu_2 - \mu^*}{\sigma_2 - \sigma^*}\right)\frac{Q^{(*2)}}{R^{(*2)}} \qquad (14)$$

with initial conditions $K^*(\sigma_1) = K_1$, $\mu^*(\sigma_1) = \mu_1$. K_1, μ_1, σ_1 are the bulk modulus, shear modulus and conductivity of the initial host material (phase 1). K_2, μ_2, σ_2 are the bulk modulus, shear modulus and conductivity of the incrementally added inclusions (phase 2). The functions $P^{(*2)}$ and $Q^{(*2)}$ and $R^{(*2)}$ are defined explicitly by Berryman (1980) for the arbitrary spheroidal inclusion, both of which depend on the effective moduli, the inclusion moduli and the inclusion aspect ratio α. The superscript $*2$ on P and Q indicates that the factors are for the inclusion of phase 2 in a background medium with effective moduli K^* and μ^*(Mavko, Mukerji and Dvorkin, 2009). As the density and velocity of brine will decrease dramatically at the supercritical state when compared with that of the subcritical state, we assume the bulk modulus for supercritical brine as 0.8 GPa. According to Kummerow et al., (2021), we set the resistivities for brine at the subcritical state and supercritical state as 5 $\Omega^{-1}m^{-1}$ and 0.5 $\Omega^{-1}m^{-1}$, respectively. The parameters for numerical modelling are listed in Table 2. Figure 3 is the calculated resistivity-moduli relation curves. When using resistivity to estimate moduli as shown in (a) and (b), the main difference is in bulk modulus, shear modulus is not influenced by fluid type. When using moduli to estimate resistivity, i.e. (c) and (d), the resistivity of the subcritical state is one order of magnitude higher than that of the supercritical state at low moduli interval (0, 20) GPa. At high moduli interval (30, 40) GPa, both states tend to be close to the grain moduli.

Table 2. Parameters used in electrical-elastic modelling, adapted from Cilli and Chapman (2021).

Constituent	K(GPa)	μ(GPa)	σ($\Omega^{-1}m^{-1}$)
Quartz	36.6	45.5	10^{-5}
Brine(subcritical)	2.29	0	5
Brine(supercritical)	0.80	0	0.5

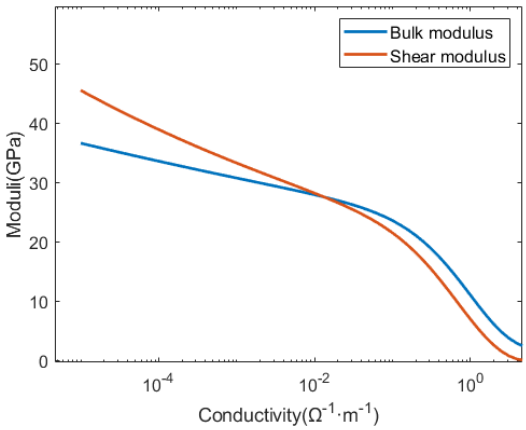

(a)Moduli calculated from resistivity (subcritical)

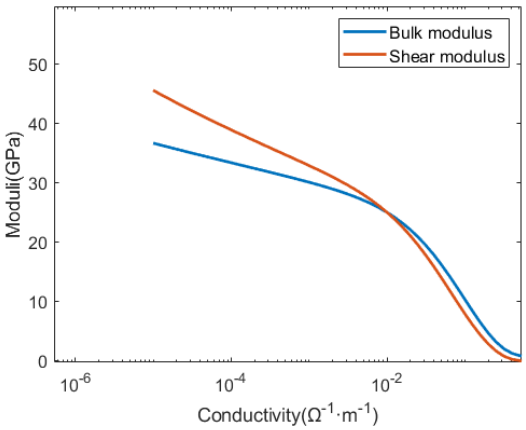

(b) Moduli calculated from resistivity (supercritical)

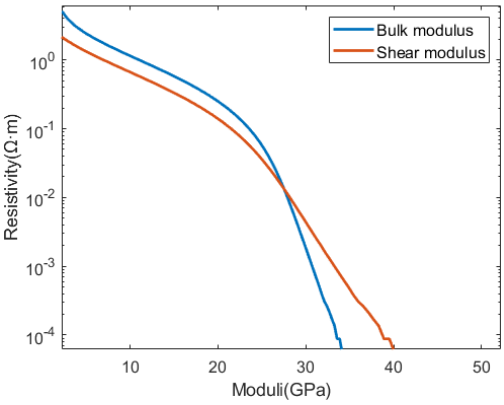

(c)Resistivity calculated from moduli (subcritical)

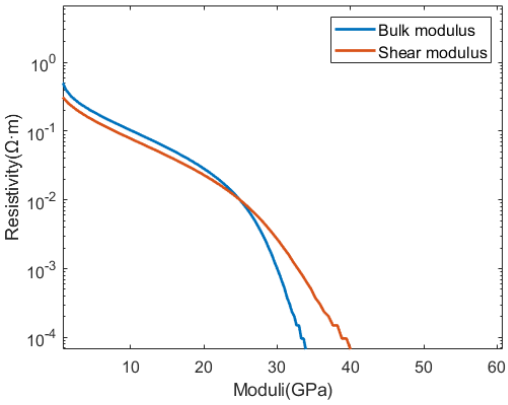

(d)Resistivity calculated from moduli (supercritical)

Figure 3. The resistivity-moduli relations calculated using the cross-property DEM model by Cilli and Chapman (2021).

2.5 BURGERS LINEAR VISCOELASTIC MODEL FOR SHEAR MODULUS

Griggs (1939) stated that creep is the slow deformation of solids under small loads acting over long periods of time. According to Singh (1975), the creep curve can be divided into three stages, i.e., primary (transient), secondary (steady state) and tertiary (accelerated). Carcione et al. (2006) proposed the use of the Burgers model to describe the linear viscoelastic creep for ductile media, where stress is not only linearly related to strain, but also depends on the time variation rate of strain. According to Carcione et al. (2014), the expression of the creep function χ in the time domain is,

$$\chi(t) = \left(\frac{t}{\eta} + \frac{1}{\mu_0}\left[1 - \left(1 - \frac{\tau_\sigma}{\tau_\epsilon}\right)\exp\left(-\frac{t}{\tau_\epsilon}\right)\right]\right) H(t). \qquad (15)$$

where t is time and $H(t)$ is the Heaviside step function. τ_σ and τ_ε are seismic relaxation times for shear deformations, μ_0 is the relaxed shear modulus, and η is the Burgers flow viscosity, which is denoted as η_B, describing the ductile behaviour related to shear deformations. The frequency-domain shear modulus μ can be obtained as $\mu_B = [F(\dot{\chi})]^{-1}$, where F denotes the time Fourier transform and a dot above a variable denotes the time derivative. It gives,

$$\mu_B(\omega) = \frac{\mu_0(1+i\omega\tau_\epsilon)}{1+i\omega\tau_\sigma - \frac{i\mu_0}{\omega\eta_B}(1+i\omega\tau_\epsilon)}. \qquad (16)$$

Alternatively, (16) can be written as,

$$\mu_B(\omega) = \mu_0\left(\frac{1+i\omega\tau_\sigma}{1+i\omega\tau_\epsilon} - \frac{i\mu_0}{\omega\eta_B}\right)^{-1}, \qquad (17)$$

where i =$\sqrt{-1}$ is the imaginary unit, and ω is the angular frequency. The limit η or $\eta_B \to \infty$ in Equation (16) or (17) recovers the Zener kernel to describe the behaviour of brittle materials,

$$\mu(\omega) = \mu_0\left(\frac{1+i\omega\tau_\epsilon}{1+i\omega\tau_\sigma}\right). \qquad (18)$$

The complex and frequency-dependent P- and S-wave velocities are,

$$v_P(\omega) = \sqrt{\frac{K+4\mu/3}{\rho}}, \text{ and } v_s(\omega) = \sqrt{\frac{\mu}{\rho}} \qquad (19)$$

K is the bulk modulus, ρ_s is the density. The shear phase velocity *c* and attenuation 1/Q are,

$$c = \left[Re(\frac{1}{v_s})\right]^{-1} \text{ and } \frac{1}{Q} = \frac{Imag(\mu)}{Real(\mu)} \qquad (20)$$

Table 3. Parameters used for the Burgers model, density and velocities are from Mavko et al. (2009) for quartz.

grain	Vp_relaxed (m/s)	Vp_unrelaxed (m/s)	Vs_relaxed (m/s)	Density (kg/m^3)	τ_ε(s)	τ_σ(s)
quartz	6050	6550	4090	2650	0.0172	0.0147

Table 3 lists the parameters used in the numerical modelling. Figure 4 shows that the complex shear modulus for the Burgers model is significantly different from that of the Zener model. For Zener model(b), the viscosity of the rock is set to be infinite, which corresponds to elastic case. We can see the typical high and low frequency bounds for the real part of moduli. For the Burgers model(a), there is a difference at the low-frequency interval of (10-100) Hz from Zener model.

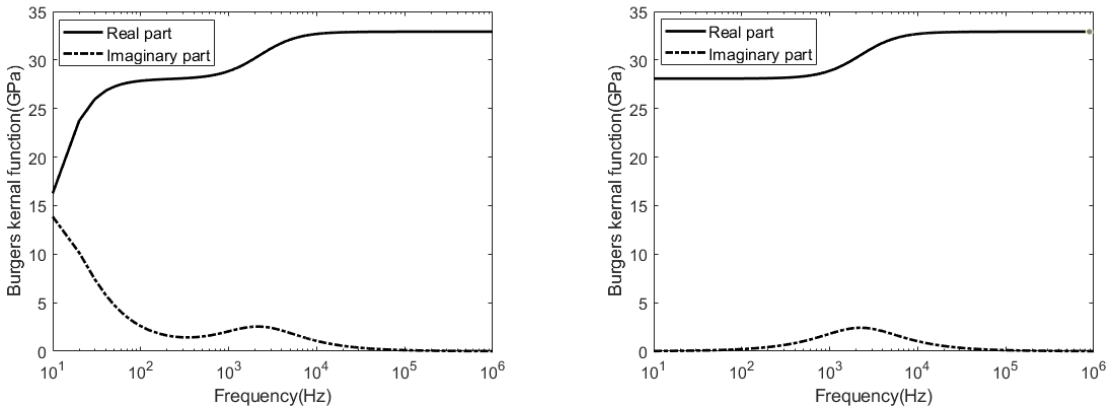

(a) Burgers model (b) Zener model

Figure 4. The complex shear modulus (kernel function) for Burgers model and Zener model.

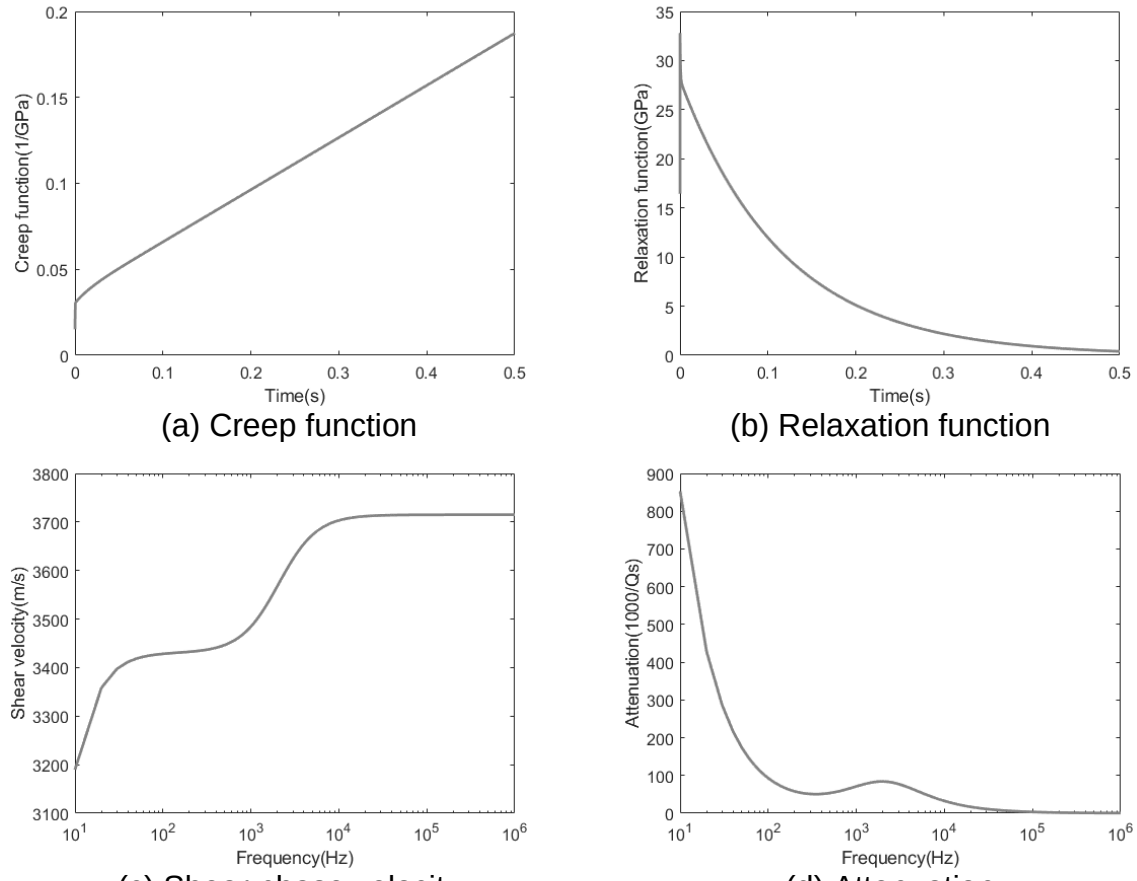

(a) Creep function (b) Relaxation function

(c) Shear phase velocity (d) Attenuation

Figure 5. The numerical modelling result for Burgers model. η_B = 5.202 $\times 10^9$ Pa·s.

Figure 5 is the numerical modelling for the Burgers model using the parameters listed in Table 3. The creep function (a) is linear, indicating a steady-state creep rate process. The relaxation function (b) tends to be zero with the increase of time. (c) and (d) are the shear wave velocity and attenuation varying with frequency, respectively.

When $\eta_B \to \infty$, it becomes the Zener model, which describes the elastic/viscoelastic behaviour of fluid-saturated rocks. As shown in Figure 6, the creep function (a) exhibits a transient response and tends to a finite asymptotic value. The relaxation function (b) shows a transient non-relaxed state, in which the system relaxes completely to the relaxation modulus with time. The shear wave phase velocity V_S and attenuation factor $1000*Q^{-1}$ are shown in (c) and (d). The attenuation model has a typical peak characteristic. The phase velocity increases with frequency from the low-frequency limit to the high-frequency limit. The system exhibits purely elastic behaviour ($Q^{-1} = 0$) at both limits.

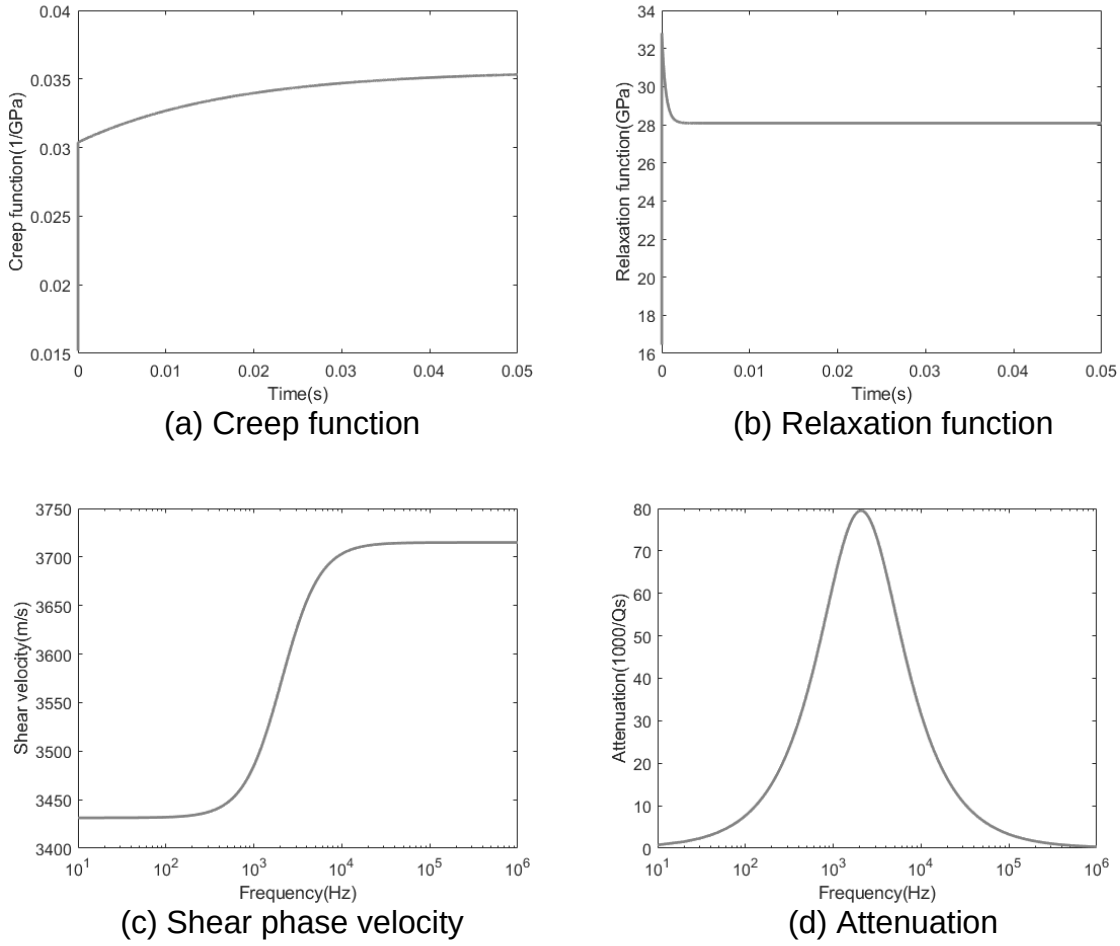

(a) Creep function (b) Relaxation function

(c) Shear phase velocity (d) Attenuation

Figure 6. The numerical modelling result for Burgers model at $\eta_B \to \infty$, which is equivalent to Zener model.

2.6 COMBINING BURGERS MODEL WITH ARRHENIUS EQUATION

According to Carcione and Poletto (2013), the viscosity η can be expressed by the Arrhenius equation as an exponential function of absolute temperature T,

$$\eta = \frac{\sigma_0}{2\dot{\epsilon}}, \quad \dot{\epsilon} = A_\infty \sigma_0^n \exp(-E/RT), \qquad (21)$$

where σ_0 is the octahedral stress given in MPa, $\dot{\epsilon}$ is the steady-state creep rate, A_∞ and n are constants, which determine the viscosity at infinite temperature together with σ_0, E is the activation energy, or the energy barrier for the rock to melt. R = 8.3144 J/mol/K is the universal gas constant. σ_0 can be defined as the following format in Cartesian coordinates,

$$\sigma_0 = \frac{1}{3}\sqrt{(\sigma_v - \sigma_h)^2 + (\sigma_v - \sigma_H)^2 + (\sigma_h - \sigma_H)^2}, \qquad (22)$$

where $\sigma_v, \sigma_H, \sigma_h$ are the vertical lithostatic stress, the maximum and minimum horizontal tectonic stresses respectively. To simplify the model, the three stress components can be estimated as,

$$\sigma_v(z) = \bar{\rho} g z, \quad \sigma_H = \frac{\upsilon \sigma_v}{1-\upsilon}, \quad \sigma_h = \xi \sigma_H, \qquad (23)$$

where $\bar{\rho}$ is the average density and g = 9.81 m/s^2 is the gravity constant. The parameter $\xi = \xi$ (x, y, z) ≤ 1 accounts for the additional effects due to tectonic stresses and $\upsilon = \upsilon$(x, y, z) is the Poisson's ratio of the formation. Assuming surface temperature is equal to zero, the temperature is a function of depth through the geothermal gradient, G, as T = zG.

Table 4. Parameters used for the Arrhenius equation from Carcione and Poletto (2013).

A_∞ ((MPa)$^{-n}$s^{-1})	E (kJ/mol)	$\bar{\rho}$ (Kg/m^3)	ξ	n	G (°C/km)	υ
10^{-2}	134	2650	0.8	2.6	60	0.2

Table 4 lists the parameters used to calculate the relation between viscosity and temperature. Figure 7 is the octahedral stress σ_0 (a) and viscosity η (b) as a function of depth and temperature. (a) shows that the octahedral stress linearly increases with temperature, while the viscosity (b) of the rock decreases with temperature. Figure 8 is the P-wave and S-wave phase velocities and quality factors as a function of temperature. From Figure 8(a), we can see phase velocities do not change with temperature before 1100°C, after which a melting zone occurs. Figure 8(b) is the P-wave and S-wave Quality factors variation with temperature. We can see a relatively lower temperature at 750°C when the values start to decrease.

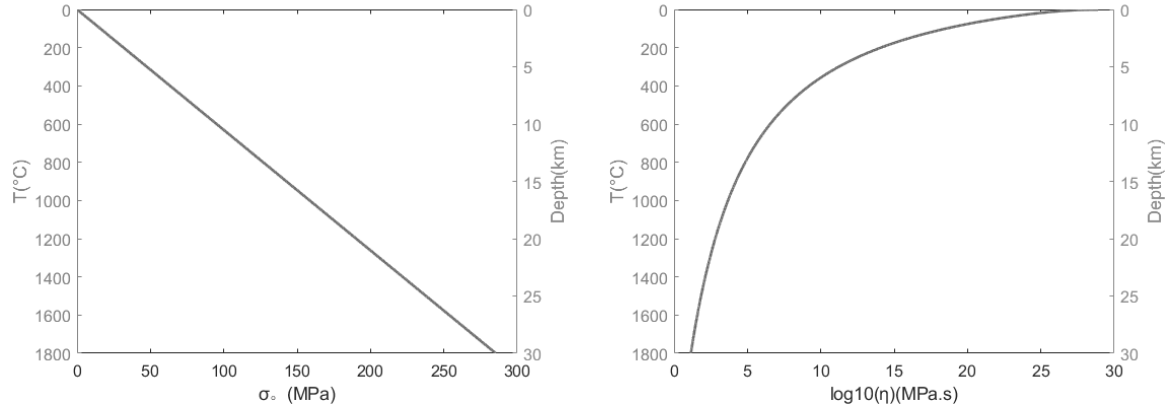

(a) σ_0 (b) η

Figure 7. Octahedral stress σ_0 (a) and viscosity η (b) as a function of depth and temperature.

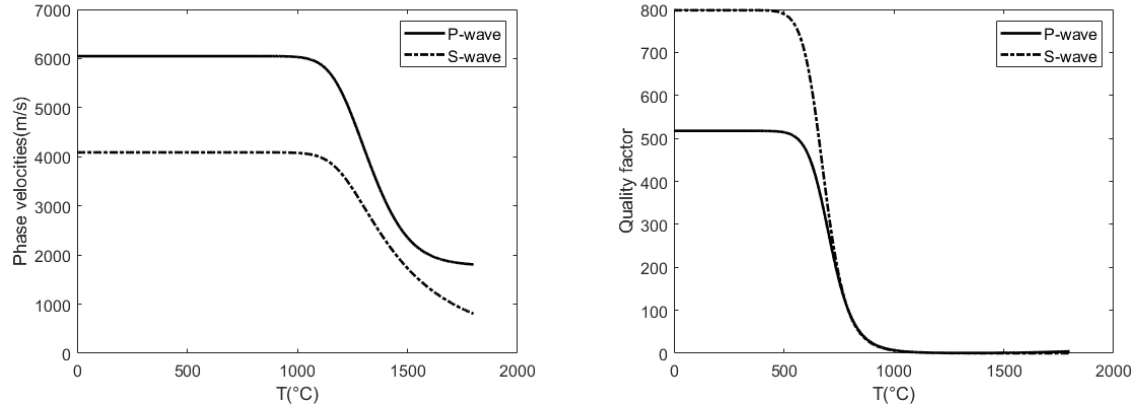

(a) Phase velocities (b) Quality factors

Figure 8. P-wave and S-wave phase velocities (a) and quality factors (b) as a function of temperature for a constant geothermal gradient and overburden density model.

2.7 COMBINING BURGERS MODEL WITH CHAPMAN ET AL. (2002) MODEL

The frequency-dependent effective bulk and shear moduli K_{eff} and μ_{eff} in Chapman et al. (2002) squirt flow model are expressed as follows:

$$K_{eff} = K - \varepsilon\left\{\frac{4(3\lambda+2\mu)(\lambda+2\mu)}{\mu(\lambda+\mu)}\left[1-3A(\omega)\right]-4\pi r A(\omega)\right\} - \phi\left\{\frac{3\lambda+2\mu}{4\mu}\left[\frac{\lambda+2\mu}{3\lambda+2\mu}+B(\omega)\right]-3B(\omega)\right\} \quad (24)$$

$$\mu_{eff} = \mu - \frac{16}{45}\varepsilon\frac{1}{1+K_c}\frac{\mu(\lambda+2\mu)}{3\lambda+4\mu}\left(K_c+\frac{1}{1+i\omega\tau}\right)-\frac{32}{45}\varepsilon\frac{\mu(\lambda+2\mu)}{3\lambda+4\mu} - \phi\frac{15\mu(\lambda+2\mu)}{9\lambda+14\mu} \quad (25)$$

where ω is the angular frequency, K, μ, λ denote the bulk and shear moduli and Lame parameter of the solid mineral matrix respectively, while the fluid bulk modulus is K_f, the total porosity is ϕ. r, a, ε are the aspect ratio, uniform crack radius and crack density of the cracks respectively. When the rock moduli at a certain frequency is measured, we can use Chapman et al. (2002) model to calculate the relaxed and unrelaxed bulk and shear moduli at low and high-frequency limits and incorporating them into the Burgers model, the fluid-saturated moduli are given by,

$$K(\omega) = \lambda(\omega) + 2\mu_B(\omega) \quad \text{and} \quad \mu(\omega) = \mu_B(\omega), \quad (26)$$

In the case of mixed steam and subcritical/supercritical water, K_f can be calculated using the Reuss (iso-stress) average of the two components (Mavko, et al., 2009),

$$K_f = \frac{1}{\frac{S_g}{K_g}+(1-S_g)/K_w}, \quad (27)$$

where S_g is the steam volume per cent, K_g is the steam bulk modulus, K_w is the subcritical/supercritical water bulk modulus. The average density of the mixed fluid ρ_f is defined by,

$$\rho_f = S_g\rho_g + (1-S_g)\rho_w, \quad (28)$$

where ρ_g, ρ_w are the density of the steam and subcritical/supercritical water, respectively. We assume a 10% porosity and 100% gas saturation for the model listed in Table 3. Figure 9 is the velocities and shear attenuation 1000/Qs varying with frequency using Chapman et al. (2002) model to calculate relaxed and unrelaxed bulk and shear moduli for Burgers model at η_B = 5.2 GPa·s and $\eta_B \to \infty$, respectively. It can be seen that at high frequencies and the transition zone, both models have the same velocities. At low frequencies, strong attenuations for P-wave and S-wave velocities occur for the Burgers model. This is due to the high viscosity of the melting rock compared with Newtonian fluids.

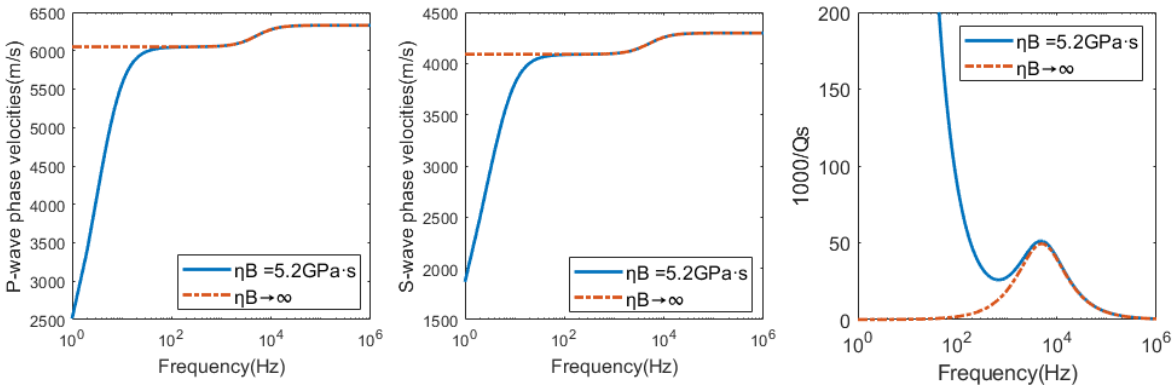

Figure 9. The velocities and attenuation curves for Burgers model at η_B = 5.2GPa·s and $\eta_B \to \infty$, which correspond to Burgers creep case and Zener elastic case, respectively. The Chapman et al. (2002) model is used to calculate the relaxed and unrelaxed elastic moduli at low and high-frequency limits.

Application of rock physics models to Aluto geothermal field

3.1 ESTIMATING THE TEMPERATURE GRADIENT FROM SEISMIC VELOCITIES

Figure 10 is the 1-D (a) P-wave and (b) S-wave velocities as a function of depth derived from 1-D earthquake data inversion at Aluto geothermal field (Wilks et al., 2020). The blue colour represents the inverted interval velocities. The red colour represents the Root-Mean-Square (RMS) velocities calculated from the interval velocities, which show a smooth trend increasing with depth. The density curve (c) is calculated using the density-velocity equation for sedimentary rocks proposed by Gardner et al. (1984),

$$\rho = 1.74 V_p^{0.25}, \qquad (29)$$

where the unit of ρ is g/cm^3, and the unit of V_p is km/s. The average density (red colour) measures the density of the overburden layer at the calculated depth. (d) is the Poisson's ratio calculated using the following equation and then transferred to average Poisson's ratio.

$$\boldsymbol{\upsilon = \frac{1}{2}\frac{(V_P/V_S)^2-2}{(V_P/V_S)^2-1}}, \qquad (30)$$

The interval velocity represents the velocity at a depth interval, is generally higher than the RMS velocity which is the root of mean square from the overburden to that depth.

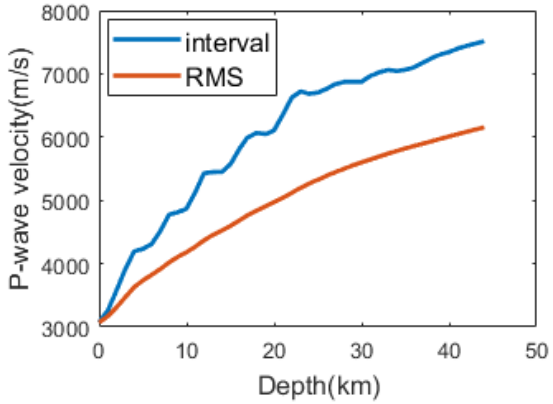

(a) P-wave velocity.

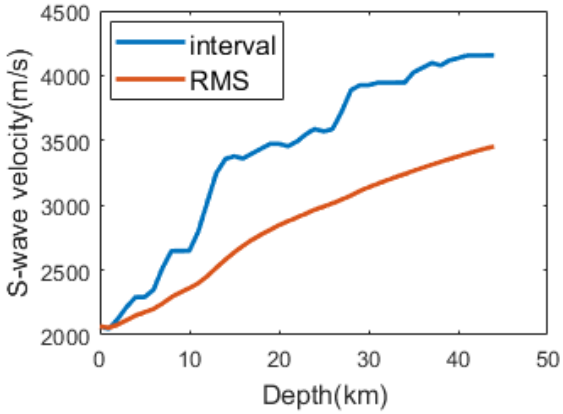

(a) S-wave velocity.

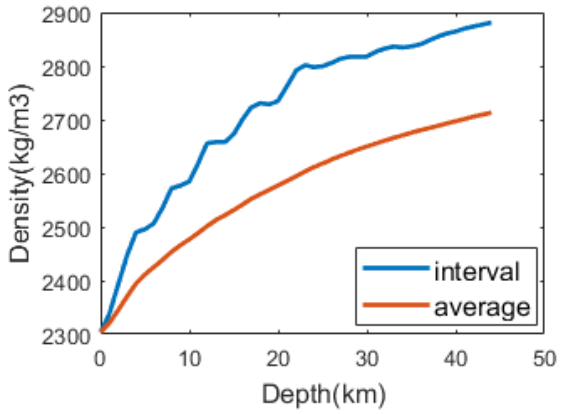

(c) The density derived from Gardner et al. (1984)'s rule.

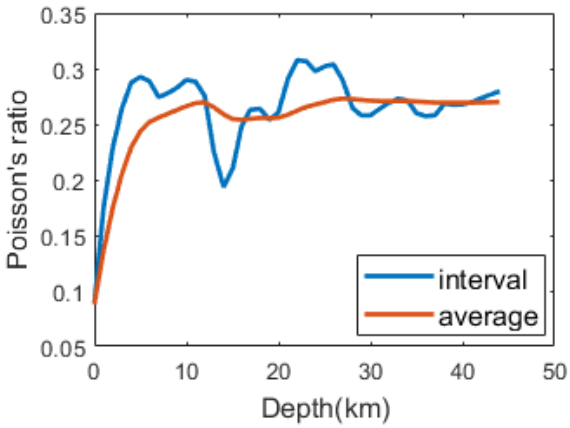

(d) The Poisson's ratio derived from velocities.

Figure 10. The P-wave (a) and S-wave (b) velocities derived from a 1-D earthquake data inversion at Aluto. The values are obtained from the supplementary materials of the Wilks et al. (2020). (c) is the density derived from the P-velocity using Gardner's rule. (d) is the Poisson's ratio derived from the velocities. Blue colour indicates interval values; Red colour indicates RMS values for velocities or average values for density and Poisson's ratio.

Figure 11 is the P-wave and S-wave velocities varying with geothermal gradient using Burgers model and Arrhenius equation. We can see that both velocities increase with depth up to about 25 km, which is different from Figure 7 when considering a constant overburden density value. However, both of the velocities are still not sensitive to temperature before 25km. A higher geothermal gradient value leads to a shallower melting zone. This is the same case for a higher A_∞ value as shown in Figure 12. When A_∞ = 0.01 after the melting zone, the P-wave velocity increases with depth again. A higher A_∞ can also reduce the melt temperature to a lower value. Figure 13 is the P-wave and S-wave velocities varying with frequency, which shows that with the increase of depth, the frequency-dependence of velocities becomes less noticeable. An ideal fitting of the P-wave and S-wave velocity curves is achieved as shown in Figure 14 using the parameters listed in Table 5, which indicates that the geothermal gradient in this area is about 40°C/km.

Table 5. Parameters used to fit the 1D P-wave and S-wave velocities in Aluto.

A_∞ ((MPa)$^{-n}$s^{-1})	E (kJ/mol)	ξ	n	G (°C/km)	f (Hz)
10^{-6}	134	0.8	2.6	40	1

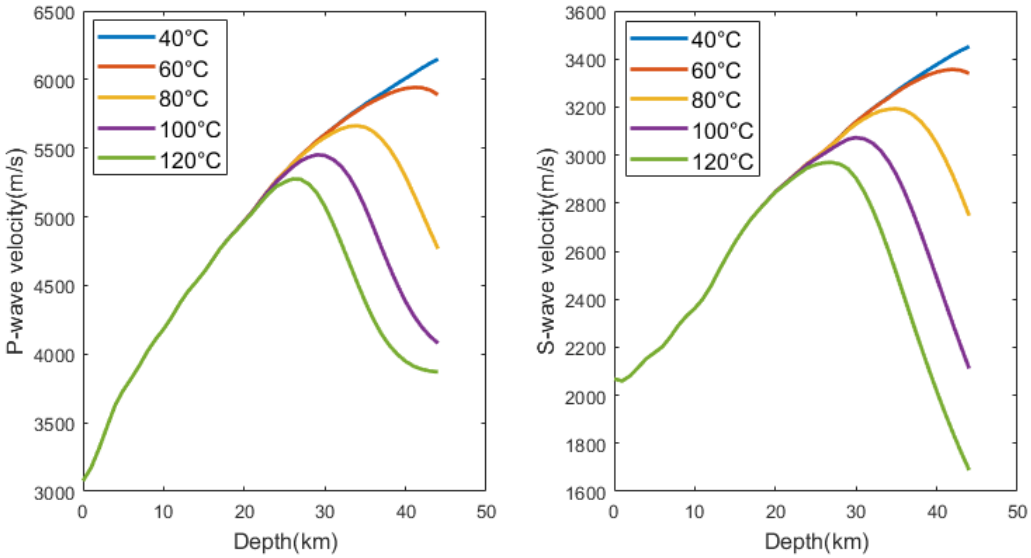

Figure 11. The calculated P-wave and S-wave velocities vary with geothermal gradient using Burgers model and Arrhenius equation.

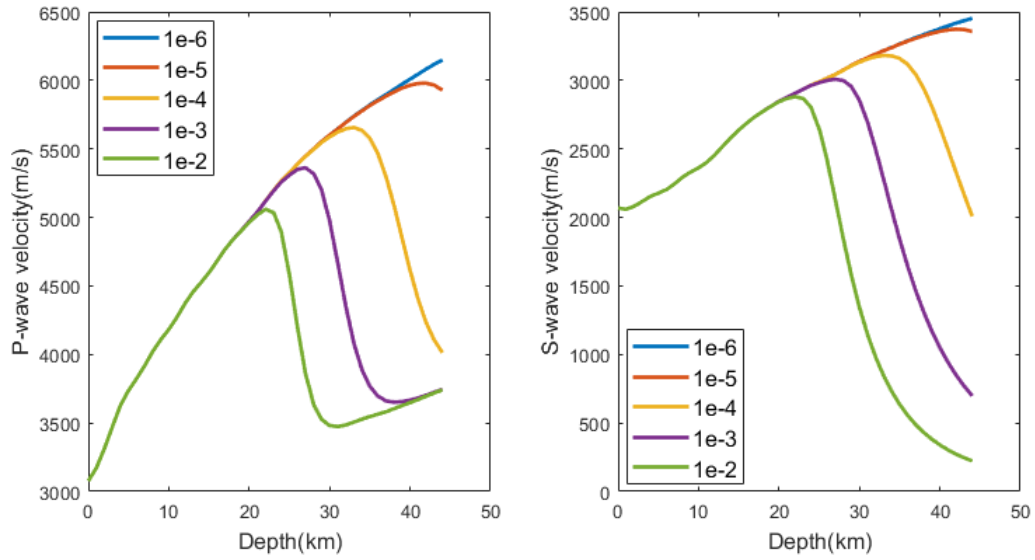

Figure 12. The calculated P-wave and S-wave velocities vary with A_∞ using Burgers model and Arrhenius equation.

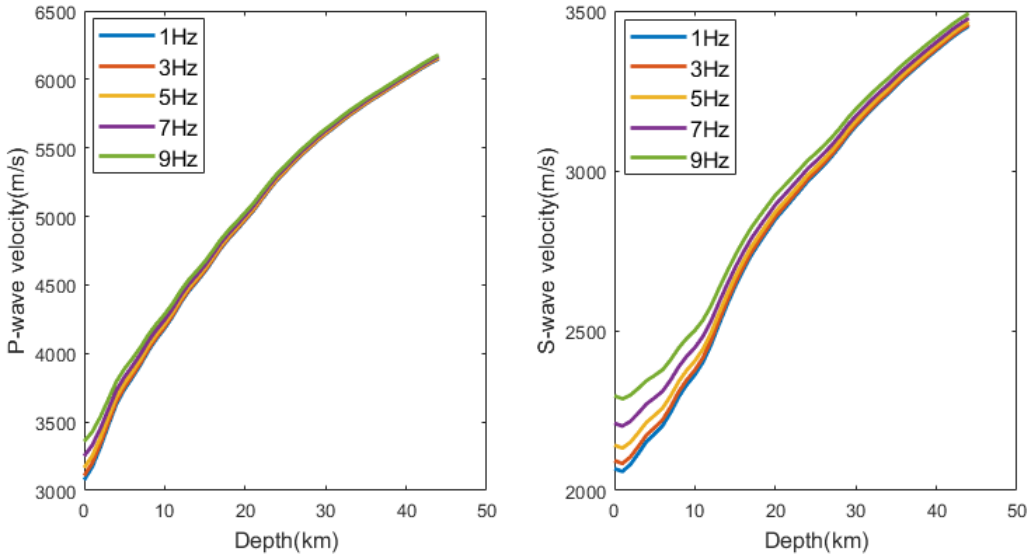

Figure 13. The calculated P-wave and S-wave velocities vary with frequency using Burgers model and Arrhenius equation.

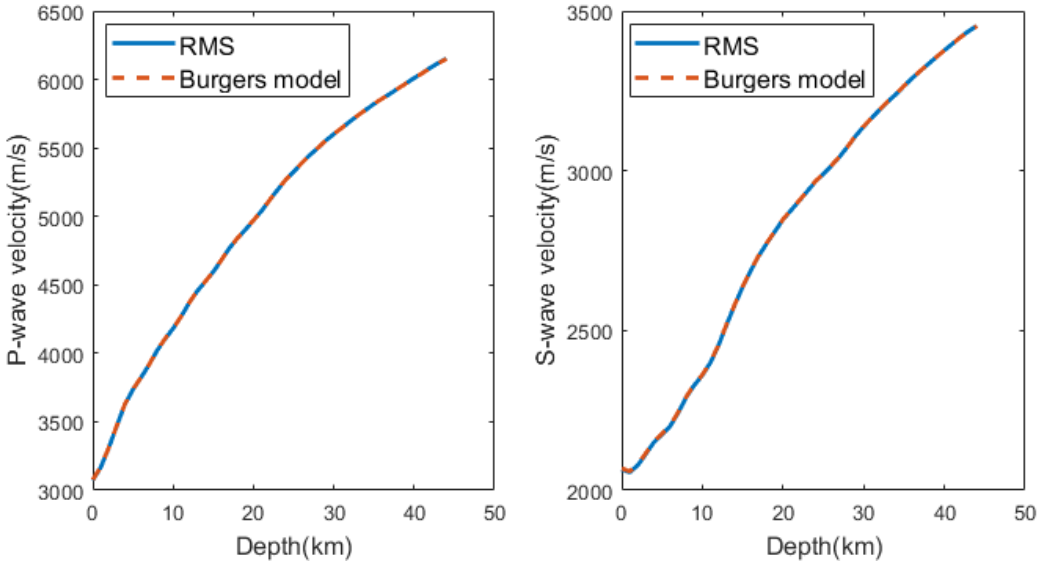

Figure 14 The fitting result using Burgers model and Arrhenius equation, which estimates the geothermal gradient G=40°C/km.

3.2 RESISTIVITY/VELOCITIES-TEMPERATURE RELATIONS

Figure 15 is a EW section across five boreholes from the 3D resistivity model by Samrock et al.(2015) in the Aluto geothermal field. According to Teklemariam et al. (1996), the abundance of clay minerals for this depth interval is illite-chlorite in LA3, which is the geothermal reservoir location. According to Gizaw (1993), LA3 is productive, being drilled into the upflow zone, while LA5 is drilled into the outflow zone. The temperature exceeds the boiling point pressure curve with a dominating gas phase at LA3.

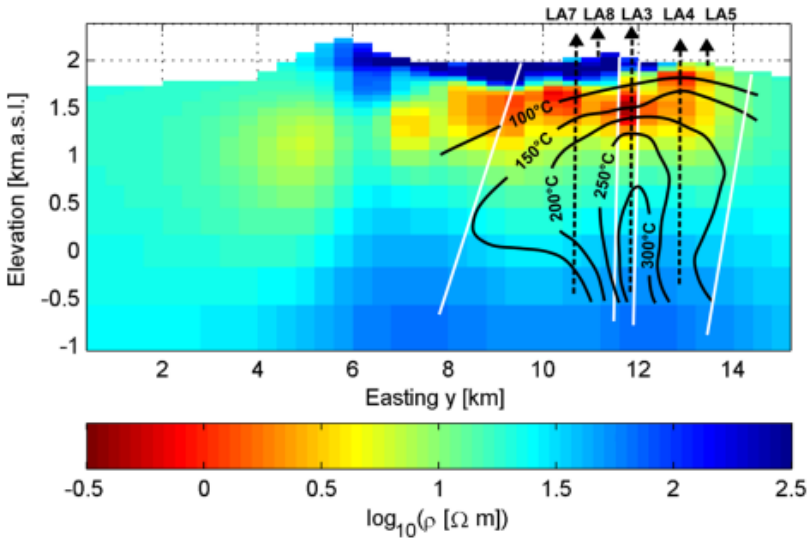

Figure 15. An EW resistivity section cited from Figure 16 of Samrock et al. (2015). The overlay temperature contours were redrawn by Samrock et al. (2015) from Gianelli & Teklemariam (1993), which was based on interpolated borehole data. The black triangles indicate the locations of boreholes. The white lines indicate the location of major faults.

Figure 16 shows the resistivity (left) and temperature (right) variation with depth between 600m-2200m at LA3 and LA5 borehole locations. The resistivities for the two boreholes increase with depth, with LA3 increasing more obviously but with values smaller than LA5. For the temperature curves, LA3 shows a small positive temperature gradient, while LA5 shows a negative gradient, which is the typical feature for upflow zone and outflow zone, respectively.

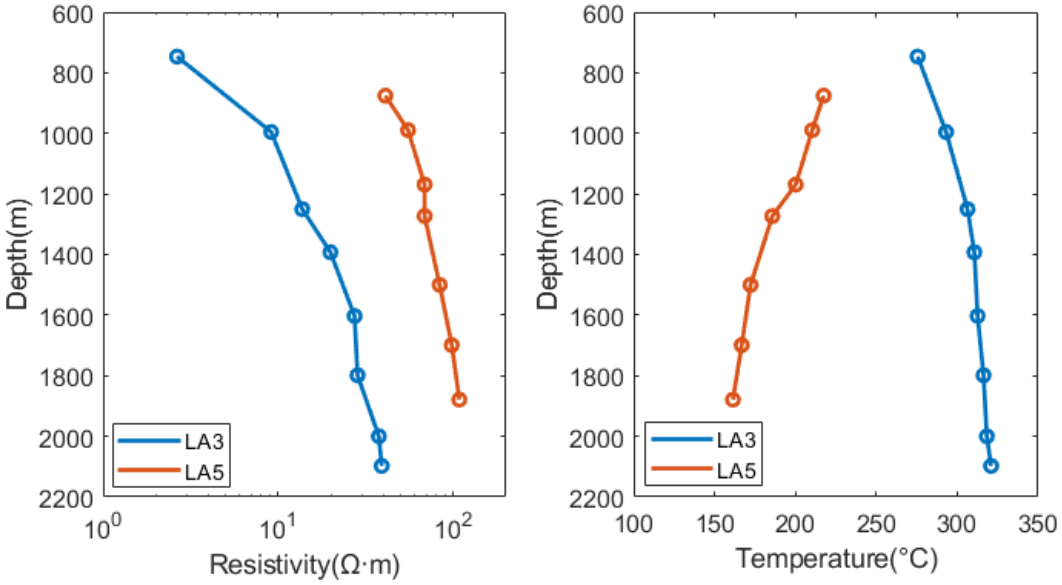

Figure 16. Left: Resistivity from 3-D model recovered by the MT data inversion at LA3 and LA5 locations. Right: Borehole temperature varying with depth at LA3 and LA5 locations. Values are taken from Figure 17 in Samrock et al. (2015). The temperature data originated from Gizaw (1993).

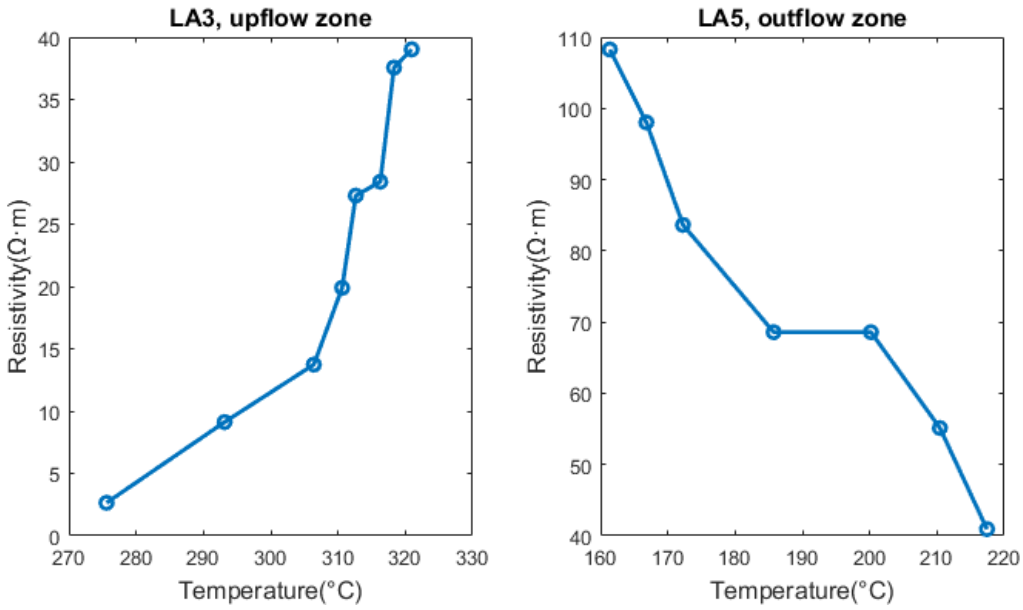

Figure 17 The subsurface temperature-resistivity relations at LA3 and LA5 locations.

Figure 17 is the subsurface temperature-resistivity relations at LA3 and LA5 locations. For LA5, a resistivity decreasing with increasing temperature can be seen with a negative temperature gradient. This is due to steam outflow at the depth between (800-1000) m, which leads to resistivity decreasing at the shallower depth. For LA3, the resistivity shows a different trend. The fluid saturation dominates the conductivity. High steam saturation due to upflow leads to high steam saturation and low resistivity at shallower depths.

In order to study how velocities vary with depth and temperature. The cross-property DEM model is used to calculate P-wave and S-wave velocities from resistivities. The following equation is used to calculate the sound speed c in water steam for LA3 and LA5.

$$c = (kp/\rho)^{1/2} = (kRT)^{1/2}\ , \qquad (31)$$

where k is the ratio of specific heat, T is the boiling point temperature, p is the boiling point pressure, R is the individual gas constant for water steam, ρ is the density. Table 6 lists the parameters used to calculate the sound speed for LA3 and LA5. Table 7 lists the moduli and resistivities for illite-chlorite clay and water steam at 200°C and 300°C, respectively.

Table 6. Parameters used to calculate the sound speed of water steam for LA3 and LA5.

Borehole name	Temperature (°C)	Pressure (bar)	Ratio of specific heat k	ρ (kg/m3)	R(J/kg·K)	sound speed (m/s)
LA5	200	15.55	1.33	7.862	461.52	538.9
LA3	300	85.92		46.21		593.1

Contain data from PipeFlow Calculations and The Engineering Toolbox websites.

Table 7. Parameters used in electrical-elastic modelling for LA3 and LA5.

Constituent	K(GPa)	μ(GPa)	ρ(Ω·m)
Illite-Chlorite	48.5	16.8	100

Water steam (200°C)	0.0023	0	1
Water steam (300°C)	0.0163	0	0.2

Figure 18 is the P-wave and S-wave moduli derived from resistivity using the cross-property DEM model at LA3 and LA5 locations. Figure 19 is subsurface temperature-velocity relations for LA3 and LA5. Figure 20 is the depth-velocity relations for LA3 and LA5.

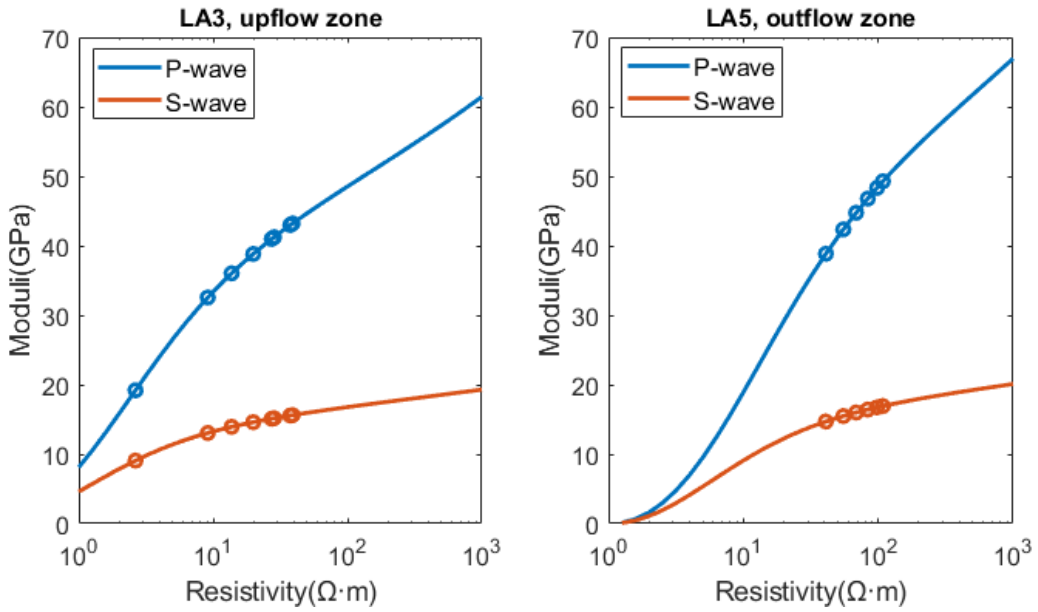

Figure 18 The P-wave and S-wave moduli derived from resistivity using the cross-property DEM model.

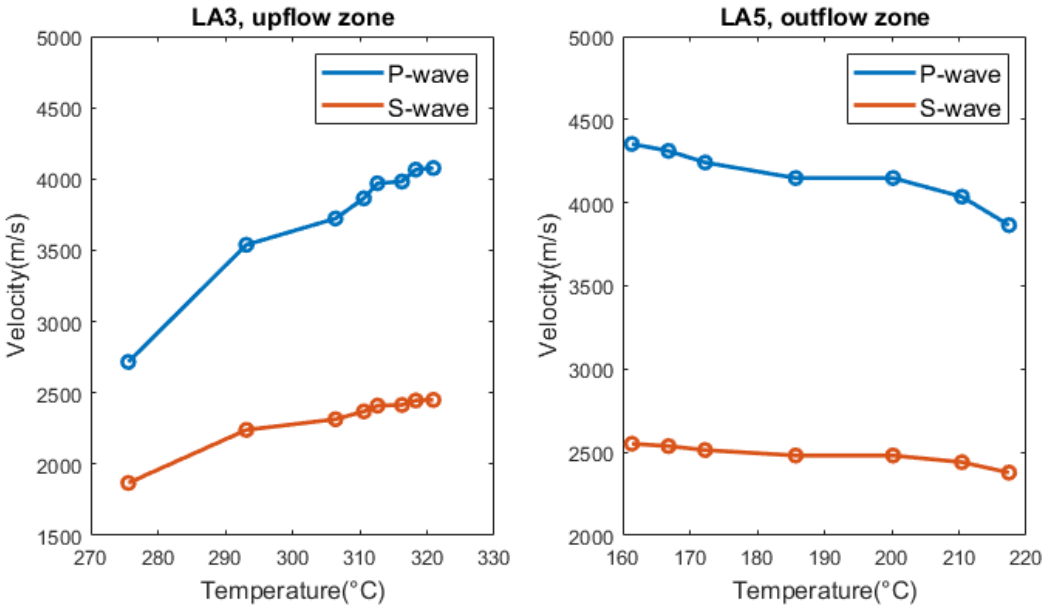

Figure 19 The temperature-velocity relations for LA3 and LA5.

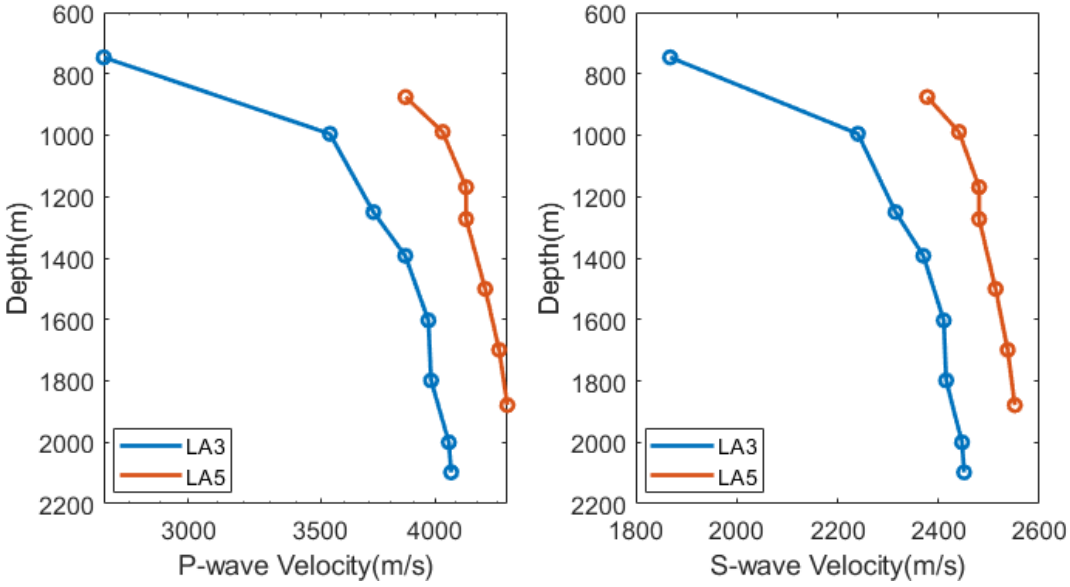

Figure 20 The depth-velocity relations for LA3 and LA5.

Discussion and conclusions

This report has introduced the empirical formulas to estimate temperature from electrical and seismic properties, and performed numerical modelling to understand the physical properties and their temperature effect for high enthalpy geothermal reservoirs. The Horner plot method can be used to estimate formation temperature from drilling data, where multiple measurements of temperature have been performed before mud circulation stops. Then the formation temperature before drilling can be extrapolated. The method is suitable when a few exploration boreholes have been drilled in the study area. Then we can estimate the temperature distribution of the subsurface section connected by boreholes through interpolation.

The Resistivity-Temperature relation $\rho_t = \rho_0 / [1+\alpha(T-T_0)]$ can be used to estimate formation temperature T from formation resistivity ρ_t, which can be obtained from the inversion of MT data. The strata profile/section needs to be divided into different lithological areas and given different initial resistivities at a certain temperature. Geological investigation is also needed to ensure that the cause of electrical resistivity difference is due to temperature before using this empirical relation. The estimated temperature field can be used to determine the location of the heat source and for borehole deployment.

Archie's law, Hermance's formula, complex refraction-index method, self-similar method, Glover et al. (2000) method, and Hashin-Strikman upper and lower bound have been studied to calculate the conductivity-porosity relation. We need to choose a suitable one according to the electric conductivity of the fluid in the study area, which affects the estimated result significantly. The combination of these equations with the Gassmann equation allows for estimating the seismic elastic properties within high-enthalpy fluid geothermal reservoirs. The cross-property DEM model can also be used to establish a direct electric-elastic properties relation and apply it to high-enthalpy geothermal reservoirs or supercritical fluid situations.

The Burgers model can be used to describe the linear viscoelastic effect of a dry hot rock frame at very high temperatures, and the forward model the variations of creep effects, seismic attenuation, velocity dispersion, and seismic response with temperature through the incorporation of the Arrhenius equation. A combination with the Chapman et al. (2002) model to calculate the relaxed and unrelaxed moduli allows the Burgers model plus Arrhenius equation to be able to estimate the geothermal gradient from depth-dependent velocities. From the application in Aluto geothermal field, we can conclude that it is possible to estimate the geothermal gradient deep to the lower crust and upper mantle using the Arrhenius equation combined with the Burgers model. The applied condition is we need to know the P-wave and S-wave velocities from the surface to a certain depth of interest so that the properties of the target geothermal reservoir and its overburden can be estimated. We also analysed the sensitivity of seismic velocities to the variation of temperature. From Figure 8, we can see velocities have no change before 1100°C. Figure 11 shows the variation between different geothermal gradients at a depth deeper than 20km, which is also at least as high as 800°C. From this, we conclude the Burgers model and Arrhenius equation are suitable to analyse melted rock and its surrounding area.

Acknowledgements

The cross-property DEM code used in this report is downloaded from: GitHub - pcilli/CP_DEM: Cross-Property DEM Toolbox, which was developed by Dr. Phil Cilli.

References

Archie, G. E., 1942, The electrical resistivity log as an aid in determining some reservoir characteristics: Petroleum Technology, 1, 55-67.

Batzle, M. and Wang, Z., 1992. Seismic properties of pore fluids. Geophysics, 57(11), pp.1396-1408.

Beggs, H.D. and Robinson, J.R., 1975. Estimating the viscosity of crude oil systems, J. Petrol. Technol., 27, 1140-1141.

Berryman, J.G., 1980. Long-wavelength propagation in composite elastic media II. Ellipsoidal inclusions, J. acoust. Soc. Am., 68(6), 1820-1831.

Berryman, J.G., 1995. Mixture theories for rock properties. Rock physics and phase relations: A handbook of physical constants, 3, pp.205-228.

Bussian, A. E., 1983, Electrical conductance in a porous medium: Geophysics, 48, 1258–1268.

Carcione, J.M., 2007. Wave fields in real media: Wave propagation in anisotropic, anelastic, porous and electromagnetic media. Elsevier.

Carcione, J.M., Helle, H. B., and Gangi, A. F., 2006. Theory of borehole stability when drilling through salt formations. Geophysics, 71, F31-F47.

Carcione, J.M., and Poletto, F., 2013. Seismic rheological model and reflection coefficients of the brittle-ductile transition. Pure Appl. Geophys., 170, 2021-2035.

Carcione, J.M., Poletto, F., and Farina, B., 2018a. The Burgers/squirt-flow seismic model of the crust and mantle. Physics of the Earth and Planetary Interiors. 274, 14-22.

Carcione, J.M., Poletto, F., Farina, B., and Bellezza, C., 2018b. 3D seismic modelling in geothermal reservoirs with a distribution of steam patch sizes, permeabilities and saturations, including ductility of the rock frame. Physics of the Earth and Planetary Interiors, 279, 67-78.

Carcione, J.M., Poletto, F., Farina, B. and Craglietto, A., 2014. Simulation of seismic waves at the Earth crust (brittle-ductile transition) based on the Burgers model, Solid Earth, 5, 1001-1010.

Carcione, J.M., Poletto, F., Farina, B., and Craglietto, A., 2016. The Gassmann-Burgers model to simulate seismic waves at the Earth crust and mantle, Pure and Applied Geophysics, 174, 849-863.

CARCIONE, J.M., URSIN, B., AND NORDSKAG, J.I., 2007, CROSS-PROPERTY RELATIONS BETWEEN ELECTRICAL CONDUCTIVITY AND THE SEISMIC VELOCITY OF ROCKS: GEOPHYSICS, 72, NO. 5, E193-E204.

CHAPMAN, M., ZATSEPIN, S.V. AND CRAMPIN, S., 2002. DERIVATION OF A MICROSTRUCTURAL POROELASTIC MODEL, GEOPHYSICAL JOURNAL INTERNATIONAL, 151, 427-451.

CHERKOSE, B.A., H. MIZUNAGA, AND F. SAMROCK. 2018. IMAGING RESISTIVITY STRUCTURES OF HIGH-ENTHALPY GEOTHERMAL SYSTEMS USING MAGNETOTELLURIC METHOD: A CASE STUDY OF ALUTO-LANGANO GEOTHERMAL FIELD IN ETHIOPIA. PROCEEDINGS, 7TH AFRICAN RIFT GEOTHERMAL CONFERENCE, KIGALI, RWANDA.

CILLI, P.A. AND CHAPMAN, M., 2020. THE POWER-LAW RELATION BETWEEN INCLUSION ASPECT RATIO AND POROSITY: IMPLICATIONS FOR ELECTRICAL AND ELASTIC MODELING, J. GEOPHYS. RES., 125(5), 1-25.

CILLI, P.A. AND CHAPMAN, M., 2021. LINKING ELASTIC AND ELECTRICAL PROPERTIES OF ROCKS USING CROSS-PROPERTY DEM. GEOPHYS. J. INT. 225, 1812-1823.

CIZ, R. AND SHAPIRO, S.A., 2007. GENERALIZATION OF GASSMANN'S EQUATIONS FOR POROUS MEDIA SATURATED WITH A SOLID MATERIAL, GEOPHYSICS,72, A75-A79.

CIZ, R., SAENGER, E.H., GUREVICH, B. AND SHAPIRO, S.A., 2009. TEMPERATURE-DEPENDENT POROELASTIC AND VISCOELASTIC EFFECTS ON MICROSCALE—MODELLING OF SEISMIC REFLECTIONS IN HEAVY OIL RESERVOIRS. GEOPHYSICAL JOURNAL INTERNATIONAL, 176(3), PP.822-832.

CUMMING W., AND MACKIE, R., 2007. 3D MT RESISTIVITY IMAGING FOR GEOTHERMAL RESOURCE ASSESSMENT AND ENVIRONMENTAL MITIGATION AT THE GLASS MOUNTAIN KGRA, CALIFORNIA, GRC TRANSACTIONS, 31, 331-334.

DAKHNOV, V. N., 1962. GEOPHYSICAL WELL LOGGING, Q. COLO. SCH. MINES, 57(2), 445.

DAVID, E. C., AND ZIMMERMAN, R. W., 2011. COMPRESSIBILITY AND SHEAR COMPLIANCE OF SPHEROIDAL PORES: EXACT DERIVATION VIA THE ESHELBY TENSOR, AND ASYMPTOTIC EXPRESSIONS IN LIMITING CASES. INTERNATIONAL JOURNAL OF SOLIDS AND STRUCTURES, 48(5), 680-688.

FARINA, B., POLETTO, F., MENDRINOS, D., CARCIONE, J.M. AND KARYTSAS, C., 2019. SEISMIC PROPERTIES IN CONDUCTIVE AND CONVECTIVE HOT AND SUPER-HOT GEOTHERMAL SYSTEMS. GEOTHERMICS, 82, PP.16-33.

GASSMANN, F., 1951. UBER DIE ELASTIZITAT POROSER MEDIEN, VIER. NATUR. GESELLSCHAFT ZURICH, 96, 1-23.

GARDNER, G. H. F., L. W. GARDNER, AND A. R. GREGORY, 1984. FORMATION VELOCITY AND DENSITY - THE DIAGNOSTIC BASICS FOR STRATIGRAPHIC TRAPS, GEOPHYSICS, 39, 770-780.

GEBRU, T.N., HARALDSDÓTTIR, S.H., HALLDÓRSDÓTTIR, S. AND GEORGSSON, L.S., 2021. ANALYSIS OF TEMPERATURE, PRESSURE AND RESERVOIR PROPERTIES, CASE STUDY OF ALUTO LANGANO GEOTHERMAL FIELD, ETHIOPIA. PROCEEDINGS WORLD GEOTHERMAL CONGRESS, REYKJAVIK, ICELAND.

GLOVER, P. W. J., M. J. HOLE, AND J. POUS, 2000, A MODIFIED ARCHIE'S LAW FOR TWO CONDUCTING PHASES: EARTH AND PLANETARY SCIENCE LETTERS, 180, 369-383.

GRIGGS, D. T., 1939, CREEP OF ROCKS: JOUR. GEOLOGY, 47, 225-251.

HAN, T., BEST, A.I., MACGREGOR, L.M., SOTHCOTT, J. AND MINSHULL, T.A., 2011. JOINT ELASTIC-ELECTRICAL EFFECTIVE MEDIUM MODELS OF RESERVOIR SANDSTONES, GEOPHYS. PROSPECT., 59(4), 777-786.

HAN, T., WEI, Z. AND LI, F., 2020. HOW THE EFFECTIVE PORE AND GRAIN SHAPES ARE CORRELATED IN BEREA SANDSTONES: IMPLICATIONS FOR JOINT ELASTIC-ELECTRICAL MODELING, GEOPHYSICS, 85(3), MR147-MR154.

HASHIN, Z., 1970. COMPLEX MODULI OF VISCOELASTIC COMPOSITES. I. GENERAL THEORY AND APPLICATION TO PARTICULATE COMPOSITES, INT. J. SOLIDS STRUC., 6, 539-552.

HERMANCE, J. F., 1979, THE ELECTRICAL CONDUCTIVITY OF MATERIALS CONTAINING PARTIAL MELT, A SIMPLE MODEL FROM ARCHIE'S LAW: GEOPHYSICAL RESEARCH LETTERS, 6, 613-616.

HORNER, D.R., 1951, PRESSURE BUILD-UP IN WELLS, PROCEEDINGS THIRD WORLD PETROLEUM CONGRESS SECTION II. LEIDEN, 503-521.

HUEBERT, J., WHALER, K., & FISSEHA, S., 2018. THE ELECTRICAL STRUCTURE OF THE CENTRAL MAIN ETHIOPIAN RIFT AS IMAGED BY MAGNETOTELLURICS: IMPLICATIONS FOR MAGMA STORAGE AND PATHWAYS. JOURNAL OF GEOPHYSICAL RESEARCH: SOLID EARTH, 123, 6019-6032.

IOVENITTI, J., SAINSBURY, J., TIBULEAC, I., KARLIN, R., WANNAMAKER, P., MARIS, V., BLACKWELL, D., THAKUR, M., IBSER, F.H., LEWICKI, J. AND KENNEDY, B.M., 2013, EGS EXPLORATION METHODOLOGY PROJECT USING THE DIXIE VALLEY GEOTHERMAL SYSTEM, NEVADA, STATUS UPDATE. IN PROCEEDINGS 38TH WORKSHOP ON GEOTHERMAL RESERVOIR ENGINEERING STANFORD UNIVERSITY, STANFORD, CALIFORNIA, FEBRUARY (PP. 11-13).

IRENA (2020), GEOTHERMAL DEVELOPMENT IN EASTERN AFRICA: RECOMMENDATIONS FOR POWER AND DIRECT USE, INTERNATIONAL RENEWABLE ENERGY AGENCY, ABU DHABI. ISBN 978-92-9260-268-0.

JAYA, M.S, SHAPIROA, S.A., KRISTINSDÓTTIRB,L.H., BRUHNC,D., MILSCHC,H., SPANGENBERGC E., 2010. TEMPERATURE DEPENDENCE OF SEISMIC PROPERTIES IN GEOTHERMAL ROCKS AT RESERVOIR CONDITIONS. GEOTHERMICS, 39, 115-123.

JONES, D., 2020. A SUMMARY OF THE EAST AFRICA RIFT TEMPERATURE AND HEAT FLOW MODEL (EARTH). BRITISH GEOLOGICAL SURVEY OPEN REPORT, OR/20/006. 24PP.

JOHNSTON, J., PELLERIN, L., HOHMANN, G., 1992. EVALUATION OF ELECTROMAGNETIC METHODS FOR GEOTHERMAL RESERVOIR DETECTION. TRANSACTIONS-GEOTHERMAL RESOURCES COUNCIL, 16, 241-245.

KUMMEROW, J., RAAB, S., A.SCHUESSLER J.A., MEYER R., 2020. NON-REACTIVE AND REACTIVE EXPERIMENTS TO DETERMINE THE ELECTRICAL CONDUCTIVITIES OF AQUEOUS GEOTHERMAL SOLUTIONS UP TO SUPERCRITICAL CONDITIONS. JOURNAL OF VOLCANOLOGY AND GEOTHERMAL RESEARCH, 391, 106388.

MAVKO, G., MUKERJI, T. AND DVORKIN, J., 2009. THE ROCK PHYSICS HANDBOOK: TOOLS FOR SEISMIC ANALYSIS OF POROUS MEDIA, 3RD EDN, CAMBRIDGE UNIV. PRESS.

MENDRINOS D., KARYTSAS C., KARYTSAS S., POLETTO F., FARINA B. AND BARISON E., 2022. CORRELATIONS OF SEISMIC VELOCITIES AND ELASTIC MODULI WITH TEMPERATURE IN SUPERHOT AND ENHANCED GEOTHERMAL SYSTEMS. CLEAN TECHNOLOGIES, 4, 440-457.

MORI T, TANAKA K., 1973. AVERAGE STRESS IN MATRIC AND AVERAGE ELASTIC ENERGY OF MATERIALS WITH MISFITTING INCLUSIONS. ACTA MATER, 21:571-574.

POLETTO, F., FARINA, B., AND CARCIONE, J. M., 2018. SENSITIVITY OF SEISMIC PROPERTIES TO TEMPERATURE VARIATIONS IN A GEOTHERMAL RESERVOIR, GEOTHERMICS, 76, 149-163.

POLETTO, F., FARINA, B., CARCIONE, J. M., AND PINNA, G., 2019. ANALYSIS OF SEISMIC WAVE PROPAGATION IN GEOTHERMAL RESERVOIRS. EUROPEAN GEOTHERMAL CONGRESS, DEN HAAG, THE NETHERLANDS.

QI, H., BA, J., AND MÜLLER, T. M., 2021. TEMPERATURE EFFECT ON THE VELOCITY-POROSITY RELATIONSHIP IN ROCKS. JOURNAL OF GEOPHYSICAL RESEARCH: SOLID EARTH, 126, E2019JB019317.

REINSCH, T., DOBSON, P., ASANUMA, H., HUENGES, E., POLETTO, F. AND SANJUAN, B., 2017. UTILIZING SUPERCRITICAL GEOTHERMAL SYSTEMS: A REVIEW OF PAST VENTURES AND ONGOING RESEARCH ACTIVITIES. GEOTHERMAL ENERGY, 5(1), PP.1-25.

SAMROCK, F., GRAYVER, A.V., CHERKOSE, B., KUVSHINOV, A. AND SAAR, M.O., 2020. ALUTO-LANGANO GEOTHERMAL FIELD, ETHIOPIA: COMPLETE IMAGE OF UNDERLYING MAGMATIC-HYDROTHERMAL SYSTEM REVEALED BY REVISED INTERPRETATION OF MAGNETOTELLURIC DATA. IN WORLD GEOTHERMAL CONGRESS (WGC 2020+1) (P. 11054). ETH ZURICH.

SAMROCK, F., KUVSHINOV, A., BAKKER, J., JACKSON, A. AND FISSEHA, S., 2015. 3-D ANALYSIS AND INTERPRETATION OF MAGNETOTELLURIC DATA FROM THE ALUTO-LANGANO GEOTHERMAL FIELD, ETHIOPIA. GEOPHYSICAL JOURNAL INTERNATIONAL, 202(3), PP.1923-1948.

SCHÖN, J. H., 1996, PHYSICAL PROPERTIES OF ROCKS: FUNDAMENTALS AND PRINCIPLES OF PETROPHYSICS. PERGAMON PRESS, INC.

SEN, P. N., C. SCALA, AND M. H. COHEN, 1981, A SELF-SIMILAR MODEL FOR SEDIMENTARY ROCKS WITH APPLICATIONS TO THE DIELECTRIC CONSTANT OF FUSED GLASS BEADS: GEOPHYSICS, 46, 781-795.

SINGH, D.P., 1975. A STUDY OF CREEP OF ROCKS. INTERNATIONAL JOURNAL OF ROCK MECHANICS AND MINING SCIENCES AND GEOMECHANICS ABSTRACTS, 12(9):271-276.

WERTHMÜLLER, D., A. ZIOLKOWSKI, AND D. WRIGHT, 2013. BACKGROUND RESISTIVITY MODEL FROM SEISMIC VELOCITIES: GEOPHYSICS, 78, NO. 4, E213-E223.

WERTHMÜLLER, D., A. ZIOLKOWSKI, AND D. WRIGHT, 2014. PREDICTING CONTROLLED-SOURCE ELECTROMAGNETIC RESPONSES FROM SEISMIC VELOCITIES. INTERPRETATION, 2(3): SH115.

WILKS, M., KENDALL, J.-M., NOWACKI, A., BIGGS, J., WOOKEY, J., BIRHANU, Y., AYELE A., BEDADA T., 2017. SEISMICITY ASSOCIATED WITH MAGMATISM, FAULTING AND GEOTHERMAL CIRCULATION AT ALUTO VOLCANO, MAIN ETHIOPIAN RIFT. JOURNAL OF VOLCANOLOGY AND GEOTHERMAL RESEARCH, 340, 52-67.

WILKS, M., RAWLINSON, N., KENDALL, J.M., NOWACKI, A., BIGGS, J., AYELE, A. AND WOOKEY, J., 2020. THE COUPLED MAGMATIC AND HYDROTHERMAL SYSTEMS OF THE RESTLESS ALUTO CALDERA, ETHIOPIA. FRONTIERS IN EARTH SCIENCE, 8, P.579699.

YANG J., FU L., ZHANG Y., AND HAN T., 2022. TEMPERATURE-AND PRESSURE-DEPENDENT PORE MICROSTRUCTURES USING STATIC AND DYNAMIC MODULI AND THEIR CORRELATION. ROCK MECHANICS AND ROCK ENGINEERING. 55, 4073-4092.

YIN T., Y. CHEN · X. LI · Q. LI, 2021. EFFECT OF HIGH TEMPERATURE AND STRAIN RATE ON THE ELASTIC MODULUS OF ROCKS: A REVIEW. INTERNATIONAL JOURNAL OF EARTH SCIENCES. 110, 2639-2660.

YUAN, H., HAN, D.H. AND ZHANG, W., 2016. HEAVY OIL SANDS MEASUREMENT AND ROCK-PHYSICS MODELING. GEOPHYSICS, 81(1), PP.D57-D70.

ZHAO G., LIU Y., HU L., BIAN K., QIN S., LIU F., AND HU, J., 2022. INVERSION OF THE TEMPERATURE AND DEPTH OF GEOTHERMAL RESERVOIRS USING CONTROLLED SOURCE AUDIO FREQUENCY MAGNETOTELLURICS AND HYDROGEOCHEMICAL METHOD. FRONTIER IN EARTH SCIENCE. 10, 858748.